



Boosting the Fischer-Tropsch synthesis performances of cobalt-based catalysts via geometric and electronic engineering: Construction of hollow structures

Weiteng Zhan^a, Yajing Wang^{a,b,*}, Jianmin Chen^a, Zhijie Chen^a, Yingwei Li^{a,c,*}

^a School of Chemistry and Chemical Engineering, South China University of Technology, Guangzhou 510640, China

^b Advanced Catalytic Engineering Research Center of the Ministry of Education, Hunan University, Changsha 410082, China

^c South China University of Technology-Zhuhai Institute of Modern Industrial Innovation, Zhuhai 519175, China

ARTICLE INFO

Keywords:

Metal-organic frameworks
Co-based catalysts
Hollow structure
Fischer-Tropsch synthesis
Nanoparticles

ABSTRACT

It is highly desirable but challenging to accelerate the dissociative adsorption of CO and lower the energy barriers of C–C coupling in the Fischer-Tropsch synthesis (FTS), both of which are prerequisite for high productivities of long-chain hydrocarbons. Herein, we report the fabrication of N-doped carbon nanotubes assembled hollow polyhedrons with embedded hollow Co (H-Co) nanoparticles (NPs) (H-Co@NCNHP) for highly efficient FTS. H-Co@NCNHP affords an extremely high C₅₊ space time yield of $1.67 \times 10^{-5} \text{ mol g}_{\text{cat}}^{-1} \text{ s}^{-1}$, outperforming most of Co-based catalysts reported to date. Theoretical calculations demonstrate that, as compared with solid Co NPs with symmetric arrangement of d-orbital electrons, H-Co NPs induce the electron rearrangement of d orbitals (especially d_{z^2}) toward the Fermi level, promoting the $d-2\pi^*/p$ coupling between Co active sites and adsorbed CO/intermediates.

1. Introduction

Fischer-Tropsch synthesis (FTS), one of the core technologies of C₁ chemistry, can transform syngas derived from coal, natural gas and biomass, into liquid fuels and chemicals [1–8]. Among the industrially significant catalysts for FTS, Co-based materials have sparked tremendous attention owing to their higher selectivities to long-chain hydrocarbons and lower activities in the side reaction of water gas shift [9–13]. However, the supported Co catalysts, which are normally prepared by the impregnation-calcination method, are prone to sinter. Thus, the maximum Co loading is less than 20 wt% [14,15]. In this context, Co-based materials derived from metal-organic frameworks (MOFs) have attracted increasing interest, by virtue of their unique features of high metal loadings, uniform distribution, and anti-sintering [16–21].

To date, improved productivities of long-chain hydrocarbons using MOFs-derived Co-based catalysts have been achieved from efforts of optimization of available cobalt sites [22,23], construction of nano-reactor [24], and fabrication of *hcp* Co nanoparticles (NPs) [18]. Compared with the Co@C obtained from the direct pyrolysis of Co-MOF [16], the silica supported Co catalysts, on which the coated graphite

shell are removed, afforded the desirable catalytic performance in FTS. Chen et al. synthesized the Co@C@SiO₂ nanoreactors through pyrolyzing ZIF-67 @SiO₂ precursors [22], which featured the characteristics of high cobalt loadings (55.6 wt%) and appropriate sizes of Co NPs (ca. 8.6 nm), exhibiting improved FTS performance. Besides, our group reported that the *fcc* Co NPs from pyrolysis of Co-MOF-71 could be partially transformed into *hcp* Co NPs, via a Co₂C intermediate, which provided a high C₅₊ space time yield (STY_{C5+}) of $1.43 \times 10^{-5} \text{ mol g}_{\text{cat}}^{-1} \text{ s}^{-1}$ [18]. In spite of the significant advances achieved, the development of Co-based catalysts for FTS still subjects to two nontrivial challenges, i. e., accelerated dissociative adsorption of CO and reduced energy barriers of C–C coupling [25], both of which are prerequisite for high productivities of long-chain hydrocarbons. In this sense, the promotion of $d-2\pi^*/p$ coupling between Co active sites and adsorbed CO/intermediates would be an ingenious strategy to overcome the above issues, by modifying the electronic structures of *d* (especially d_{z^2}) orbitals in Co NPs.

In this work, we developed a simple and effective “pyrolysis-oxidation-reduction” strategy to construct H-Co NPs, which are embedded in N-doped carbon nanotubes (NCNTs) of hollow polyhedrons (H-Co@NCNHP). Benefiting from the integrating merits of modified empty/

* Corresponding authors at: School of Chemistry and Chemical Engineering, South China University of Technology, Guangzhou 510640, China.

E-mail addresses: wangyj4302@scut.edu.cn (Y. Wang), liyw@scut.edu.cn (Y. Li).

<https://doi.org/10.1016/j.apcatb.2022.121469>

Received 2 March 2022; Received in revised form 18 April 2022; Accepted 29 April 2022

Available online 3 May 2022

0926-3373/© 2022 Elsevier B.V. All rights reserved.

occupied d_{z^2} orbitals and up-shifted d -band center in H-Co NPs and hollow polyhedron, the optimal H-Co@NCNHP material presents super catalytic performances in FTS with a STY_{C5+} value as high as $1.67 \times 10^{-5} \text{ mol g}_{\text{cat}}^{-1} \text{ s}^{-1}$. Moreover, H-Co@NCNHP behaves good stability within 120 h of reaction. We envision that the design concept about the integration of geometric and electronic engineering could inspire new exploration and insights in fabricating distinctive FTS catalysts with targeted functionalities.

2. Experimental section

2.1. Chemicals

All chemicals used in this work were analytical grade and purchased from commercial suppliers and used without any further treatments.

2.2. Materials preparation

2.2.1. Synthesis of ZIF-67

$\text{Co}(\text{NO}_3)_2 \cdot 6\text{H}_2\text{O}$ (875.4 mg, 3 mmol) and 2-methylimidazole (2-MeIm) (990 mg, 12 mmol) were dissolved in 75 mL of methanol with ultrasonic treatment, respectively. Then the methanolic solution of $\text{Co}(\text{NO}_3)_2 \cdot 6\text{H}_2\text{O}$ was poured into the solution of 2-MeIm and stirred vigorously for 10 min. After aging for 24 h at room temperature, the resulting purple product was collected by centrifugation and washed with methanol for several times. Finally, the product was dried at 60 °C.

2.2.2. Synthesis of S-Co@NCNHP

A quartz boat loaded with ZIF-67 was placed in a tubular furnace and pyrolyzed at 600 °C for 3 h with a heating rate of 2 °C min^{-1} in a flow of H_2/Ar ($V_{\text{H}_2}:V_{\text{Ar}} = 1:9$). The solid Co NPs are confined in the tips of NCNTs, which are assembled into hollow polyhedron (denoted as S-Co@NCNHP).

2.2.3. Synthesis of H- Co_3O_4 @NCNHP

A quartz boat loaded with ZIF-67 was placed in a tubular furnace and pyrolyzed at 600 °C for 3 h with a heating rate of 2 °C min^{-1} in a flow of H_2/Ar ($V_{\text{H}_2}:V_{\text{Ar}} = 1:9$). After cooling to 250 °C, the atmosphere was changed to O_2/Ar ($V_{\text{O}_2}:V_{\text{Ar}} = 3:97$) and held for 1 h. The hollow Co_3O_4 NPs are confined in the tips of NCNTs, which are assembled into hollow polyhedron (denoted as H- Co_3O_4 @NCNHP).

2.2.4. Synthesis of H-Co@NCNHP

A quartz boat loaded with ZIF-67 was placed in a tubular furnace and pyrolyzed at 600 °C for 3 h with a heating rate of 2 °C min^{-1} in a flow of H_2/Ar ($V_{\text{H}_2}:V_{\text{Ar}} = 1:9$) atmosphere. After cooling to 250 °C, the atmosphere was changed to O_2/Ar ($V_{\text{O}_2}:V_{\text{Ar}} = 3:97$) and held for 1 h. Finally, the sample was further reduced at 350 °C for 3 h in a flow of H_2/Ar ($V_{\text{H}_2}:V_{\text{Ar}} = 1:9$). The hollow Co NPs are confined in the tips of NCNTs, which are assembled into hollow polyhedron (denoted as H-Co@NCNHP).

2.2.5. Synthesis of H-Co@NCNSP

A quartz boat loaded with ZIF-67 was placed in a tubular furnace and pyrolyzed at 600 °C for 3 h with a heating rate of 2 °C min^{-1} in a flow of Ar. After cooling to 250 °C, the atmosphere was changed to O_2/Ar ($V_{\text{O}_2}:V_{\text{Ar}} = 3:97$) and held for 1 h. Finally, the sample was further reduced at 350 °C for 3 h in a flow of H_2/Ar ($V_{\text{H}_2}:V_{\text{Ar}} = 1:9$). The hollow Co NPs are confined in the tips of NCNTs, which are assembled into solid polyhedron (denoted as H-Co@NCNSP).

2.2.6. Synthesis of S-Co@NCSP

A quartz boat loaded with ZIF-67 was placed in a tubular furnace and pyrolyzed at 600 °C for 3 h with a heating rate of 2 °C min^{-1} in a flow of Ar. The solid Co NPs are embedded in N-doped carbon, which are assembled into solid polyhedron (denoted as S-Co@NCSP).

2.2.7. Synthesis of S-Co/C

The active carbon was impregnated into $\text{Co}(\text{NO}_3)_2 \cdot 6\text{H}_2\text{O}$ aqueous solution under stirring at room temperature until dried. And then the sample was pyrolyzed at 600 °C for 3 h in a flow of H_2/Ar ($V_{\text{H}_2}:V_{\text{Ar}} = 1:9$) to obtain S-Co/C.

2.3. Characterizations

X-ray diffraction (XRD) patterns of various catalysts were recorded on a Rigaku diffractometer (D/MAX-III A, 3 kW) by using Cu K α radiation (40 kV, 40 mA, $\lambda = 0.1543 \text{ nm}$). The specific surface areas and pore sizes were obtained by N_2 adsorption/desorption measurements at 77 K with a Micromeritics ASAP 2020 M instrument. Before the measurement, the sample was degassed at 150 °C for 6 h. X-ray photoelectron spectroscopy (XPS) was employed to measure the electronic states of surface elements with a Thermo Scientific Escalab 250Xi system (2×10^{-9} torr). The metal contents of the catalysts were analyzed by the inductively coupled plasma optical emission spectrometry (ICP-OES) on an Optima 8300 instrument. The morphologies of catalysts were investigated by scanning electron microscopy (SEM, HITACHI SU8220). The high-resolution transmission electron images, high-angle annular dark-field scanning TEM (HAADF-STEM), and elemental mapping were acquired on a transmission electron microscopy (TEM, JEOL 2100F) at 200 kV. The content of N was analyzed by an Elementar Vario EL III equipment.

In situ diffuse reflection infrared Fourier-transform (DRIFT) measurements were carried out on a Bruker TENSOR II equipment with MCT detector. Typically, the catalysts were first degassed under vacuum at 150 °C for 6 h. Then the samples inside the cell were purged by an Ar flow (25 mL min^{-1}) from room temperature to 230 °C, at which the background spectra were acquired. Subsequently, Ar was switched to syngas, and the spectra were collected after 0.5 h. After that, the samples were purged with Ar for 0.5 h, and the spectra were collected again.

H_2 temperature-programmed reduction (H_2 -TPR) and temperature-programmed desorption (H_2 -TPD) were performed on a HUASI instrument (DAS-7200). For the H_2 -TPR measurements, 100 mg of sample was pretreated under a flow of Ar at 200 °C for 2 h. After cooling down to 50 °C, the sample was heated to 600 °C under a flow of H_2/Ar ($V_{\text{H}_2}:V_{\text{Ar}} = 1:9$) with a heating rate of 10 °C min^{-1} , and meanwhile, the H_2 reduction profile was recorded by a TCD detector. For the H_2 -TPD measurements, 100 mg of sample was pretreated at 200 °C for 2 h under Ar atmosphere. After cooling down to 50 °C, the atmosphere was changed to H_2/Ar and held for 1 h, after which Ar flow was introduced to remove the physically adsorbed molecules. Then the temperature was increased to 600 °C with a heating rate of 10 °C min^{-1} , and meanwhile, the H_2 desorption profile was recorded.

For the CO temperature-programmed desorption (CO-TPD) measurements, 100 mg of catalyst was pretreated under a flow of Ar at 200 °C for 2 h with a heating rate of 10 °C min^{-1} . After cooling down to 50 °C, the atmosphere was changed to CO/He flow ($V_{\text{CO}}:V_{\text{He}} = 1:9$) and held for 1 h, after which Ar flow was introduced to remove the physically adsorbed molecules. Then the temperature was enhanced to 600 °C at a heating rate of 10 °C min^{-1} , and meanwhile, the signal of CO ($m/z = 28$) was recorded by a mass spectrometer (MS).

X-ray absorption fine structure (XAFS) technique was used to investigate the electronic properties and local chemical environment of Co species of samples. XAFS experiments of Co K -edge were carried out at the BL14W1 station of Shanghai Synchrotron Radiation Facility. Before the measurements, samples were evenly coated on the 3 M tape. Typical XAFS spectra of Co K -edge were collected in the range of 7505–8483 eV. The XAFS spectra of all samples were accurately calibrated by simultaneously recording that of standard Co foil, collecting in transmission mode. XAFS data processing was done by using the Demeter program. The k^3 -weighted Co K -edge EXAFS oscillations were Fourier-transformed within 3.0–13.0 \AA^{-1} , using Hanning window with $\Delta k = 1.0 \text{ \AA}^{-1}$. The EXAFS oscillations were fitted in the R space (without

phase correction) over a radial distance range of 1.0–2.7 Å to extract the structural parameters (coordination numbers, interatomic distances, and disorder degrees), with application of k^1 and k^3 weighting. The Wavelet transform (WT) EXAFS was acquired based on the protocol of Morlet wavelets by using the Fortran software.

2.4. Catalytic tests

The FTS was carried out in a fixed-bed micro-reactor (9 mm i.d. and 300 mm length). Typically, 0.5 g of catalyst (40–60 mesh) was first mixed with quartz sands in a mass ratio of 1:4. A premixed syngas in a cylinder ($V_{H_2}:V_{CO}:V_{Ar} = 64:32:4$) was introduced into the reactor, in which Ar was employed as an internal standard to analyze gaseous products monitored by a gas chromatography (GC, PANNA A91). Liquid products and wax collected in a cold trap and a hot trap, respectively, were off-line analyzed by an Agilent GC-MS (5977 A MSD). Samples were first activated in-situ in a flow of H_2/Ar ($V_{H_2}:V_{Ar} = 1:9$) at 400 °C for 3 h. The reaction was operated at 230 °C and 2 MPa, with a gas velocity of 30 mL min⁻¹ (gas hour space velocity (GHSV = 3600 mL g_{cat}⁻¹ h⁻¹)), unless otherwise noted. Carbon balance was higher than 95% and the hydrocarbon selectivities were reported excluding CO₂.

CO conversion was calculated according to the following equation.

$$X_{CO}(\%) = \frac{CO_{in} - CO_{out}}{CO_{in}} \times 100\% \quad (1)$$

where CO_{in} and CO_{out} denote moles of CO at the inlet and outlet, respectively.

CO₂ selectivity was calculated according to the following equation.

$$S_{CO_2}(\%) = \frac{CO_{2,out}}{CO_{in} - CO_{out}} \times 100\% \quad (2)$$

where $CO_{2,out}$ denotes moles of CO₂ at the outlet.

The selectivity of hydrocarbons with different carbon numbers was calculated according to the following equation.

$$S_{C_n}(\%) = \frac{nC_{n,out}}{\sum_1^n nC_{n,out}} \times 100\% \quad (3)$$

where $C_{n,out}$ denotes moles of C_n at the outlet.

The carbon chain growth probability (α) was calculated according to the following equation.

$$\ln \frac{W_n}{n} = n \ln \alpha + \ln \frac{(1 - \alpha)}{\alpha} \quad (4)$$

where W_n is the weight fractions of the hydrocarbon products with a carbon number of n .

The turnover frequency (TOF) and STY_{C5+} of different catalysts were calculated according to the following equations.

$$TOF = \frac{F_{CO} \times X_{CO} \times M_{Co}}{m_{cat} \times w_{Co} \times V_m \times D_{Co} \times 3600} \quad (5)$$

$$STY_{C5+} = \frac{F_{CO} \times X_{CO}}{m_{cat} \times V_m \times 3600} \times S_{C5+} \quad (6)$$

where F_{CO} is the velocity of CO (L h⁻¹), X_{CO} is the CO conversion, M_{Co} is the molar mass of Co (g mol⁻¹), m_{cat} is the mass of catalyst (g), w_{Co} is the mass fraction of Co, V_m is the molar volume of gas (L mol⁻¹), and D_{Co} is the metallic Co dispersion corrected by reducibility.

2.5. Computational details

Density Functional Theory (DFT) calculations were implemented using pseudopotential plane wave method and CI-NEB one, available in Quantum espresso [26,27]. The Perdew-Bueke-Ernzerhof (PBE) functional [28] and Projected augmented wave (PAW) potentials [29] were

used to describe the exchange-correlation effects of electrons and the ionic cores, respectively. Two frustum models were used to mimic solid and hollow spherical Co NPs. During the geometry optimizations, all the atom positions were allowed to relax. In this work, the Brillouin-zone sampling was conducted using Monkhorst-Pack (MP) [30] grids of special points with the separation of 0.04 Å⁻¹. The convergence criterion for the electronic self-consistent field (SCF) loop was set to be 1×10^{-5} eV. The optimized structures were obtained until the residual forces were below 0.05 eV Å⁻¹.

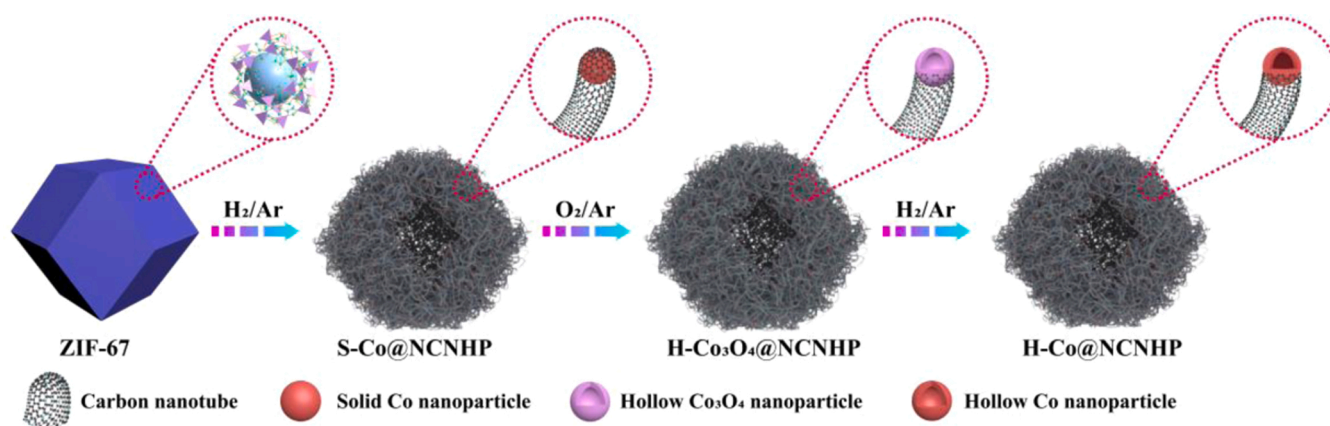
3. Results and discussion

3.1. Fabrication and structural properties of the materials

The fabrication process of H-Co@NCNHP, via a pyrolysis-oxidation-reduction strategy, is schematically illustrated in Scheme 1. First, uniform ZIF-67 rhombic dodecahedrons (ca. 1 μm) were synthesized (Fig. S1). The pyrolysis of ZIF-67 gave S-Co@NCNHP under 10% H_2/Ar atmosphere at 600 °C. Metallic Co NPs could be quickly formed in the H_2 atmosphere, which could catalyze the growth of NCNTs. The fast pyrolysis of ligands and gradual consumption of C for the growth of NCNTs occur simultaneously, forming the inner hollow structure of carbon polyhedron. As observed in Fig. S2, solid Co (S-Co) NPs (ca. 16.6 nm) are confined in the tips of NCNTs, which are assembled into hollow polyhedron. Upon the subsequent oxidation treatment under 3% O_2/Ar atmosphere at 250 °C, H-Co₃O₄@NCNHP was obtained, and the morphological and structural evolution of S-Co@NCNHP to H-Co₃O₄@NCNHP is shown in Fig. S3. With an increase in the oxidation time, the S-Co NPs are gradually transformed into yolk-shelled (at 40 min) and then hollow (at 60 min) Co₃O₄ NPs, both of which are semi-embedded in NCNTs, due to the Kirkendall effect [31]. As the precursor was treated in O_2/Ar atmosphere, some C will be oxidized and released in the form of oxides of carbon. Therefore, the carbon layers covered on the tips of Co₃O₄ NPs are largely removed after oxidation. Such an elaborate oxidation treatment is favorable for increasing the number of accessible Co atoms and also for the subsequent construction of H-Co NPs.

The as-prepared H-Co₃O₄@NCNHP was then subjected to reduction at 350 °C under 10% H_2/Ar (Figs. 1 and S4–S5). The ideal H-Co@NCNHP could be obtained at the reduction time of 3 h, showing well-preserved hollow polyhedrons assembled by NCNTs (Fig. 1a–d, f, g). The elemental mapping (Fig. 1e) evidences the even distribution of Co, C, and N elements throughout the hollow polyhedron. A close inspection of hollow NPs (ca. 17.3 nm) embedded in NCNTs (Fig. 1h) exhibits lattice fringes spaced by 0.203 nm, which are attributed to the (111) plane of Co (PDF#15-0806), in good agreement with the XRD results (Fig. 1i). These results substantiate that we have successfully fabricated the H-Co@NCNHP material via a novel pyrolysis-oxidation-reduction strategy.

In order to highlight the unique advantages of the H-Co@NCNHP material, some comparative samples including S-Co@NCNHP, H-Co@NCNSP, S-Co@NCSP, and S-Co were also prepared. The synthesis processes are schematically illustrated in Scheme S1. All the corresponding characterization results verify the successful fabrication of these Co-based materials with different structures (Figs. S2 and S6–S8). The BET surface areas of H-Co@NCNHP, H-Co@NCNSP, S-Co@NCNHP, and S-Co@NCSP are 186.8, 186.0, 270.2, and 213.6 m² g⁻¹, respectively, as measured by N₂ adsorption-desorption experiments (Fig. S9). The high specific surface areas and highly porous structures of all the catalysts would be beneficial for mass transport and accessibility of active sites [32]. To measure the electronic states of surface Co species of different Co-based catalysts, XPS analysis was performed. As observed in Fig. S10, the Co 2p_{3/2} spectra of samples could be deconvoluted into four peaks located at ca. 778.5, 780.2, 782.3, and 785.8 eV, corresponding to Co, Co-O_x, Co-N, and satellite peaks, respectively. The presence of Co-O_x species is attributed to the inevitable oxidation of surfaces of Co NPs in air.



Scheme 1. Fabrication strategy of H-Co@NCNHP.

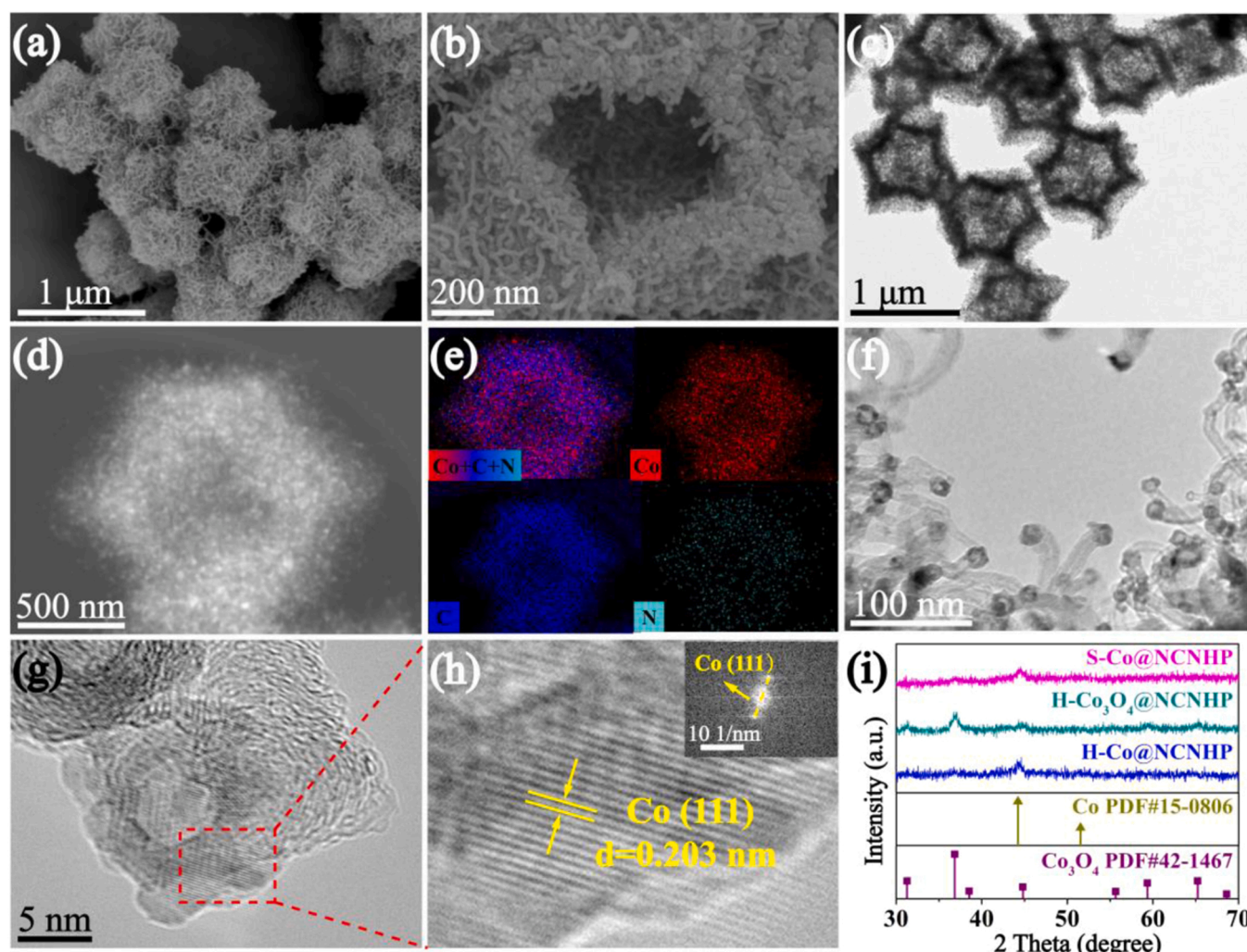


Fig. 1. (a, b) SEM, (c, f) TEM, (d) HAADF-STEM images, (e) EDX mapping and (g, h) high-magnification TEM images of H-Co@NCNHP. The inset of (h) is the FFT pattern. (i) XRD patterns of S-Co@NCNHP, H-Co₃O₄@NCNHP, and H-Co@NCNHP.

To investigate the differences in both electronic structure and local coordination environment of H-Co and S-Co NPs, two representative materials (S-Co@NCNHP and H-Co@NCNHP) were examined by X-ray absorption near-edge structure (XANES) and extended X-ray absorption fine structure (EXAFS) measurements. The XANES spectra of Co *K*-edge (Fig. 2a) show that the curves of H-Co@NCNHP and S-Co@NCNHP are

well in accordance with that of Co foil, implying that the Co species are almost completely reduced. These results could also be evidenced by the observation of the dominating peaks at ca. 2.50 Å, which are attributed to the contribution of Co–Co (Fig. 2b). Besides, the WT contour plots of S-Co@NCNHP and H-Co@NCNHP display only one maximum intensity at 6.8 Å^{−1}, associated with Co–Co coordination shells (Fig. 2c).

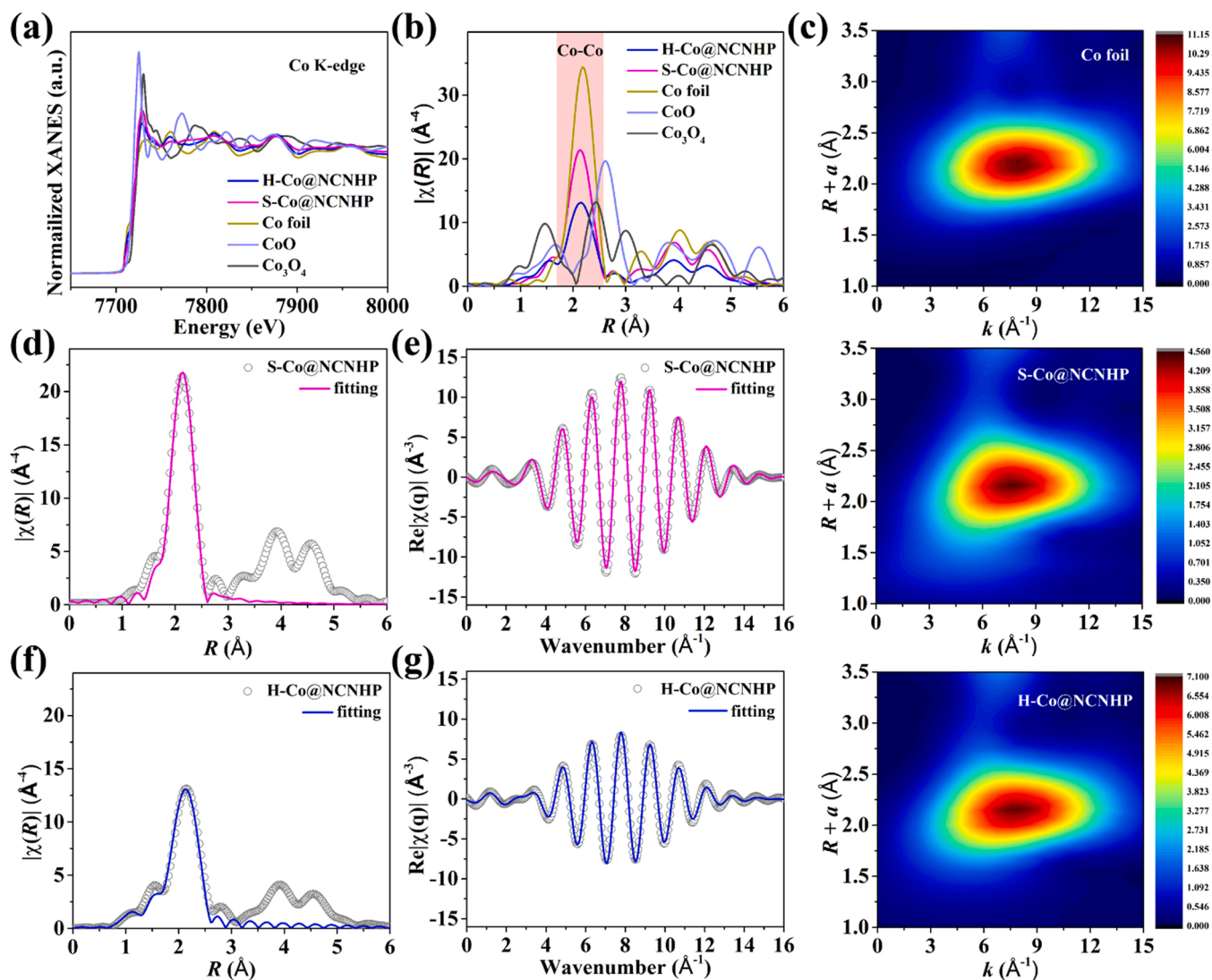


Fig. 2. (a) Co K-edge XANES spectra and (b) FT of k^3 -weighted Co K-edge EXAFS spectra (without phase correction) for Co foil, CoO, Co_3O_4 , S-Co@NCNHP, and H-Co@NCNHP. (c) Co K-edge WT-EXAFS contour plots for Co foil, S-Co@NCNHP, and H-Co@NCNHP. Co K-edge EXAFS fitting spectra for S-Co@NCNHP and H-Co@NCNHP in (d, f) R space and (e, g) q space.

According to the EXAFS fitting results (Table S1), the coordination numbers (C.N.) of Co–Co coordination shells of S-Co@NCNHP and H-Co@NCNHP are 6.9 and 4.2, respectively. This suggests that H-Co NPs could afford an increased localization of the valence electrons, strengthening the bonds between Co active sites and adsorbates [33].

3.2. Catalytic performances in FTS

Intrigued by the fascinating features of H-Co@NCNHP materials, we then investigated their catalytic performances in FTS. The effect of reaction temperature on CO conversion and hydrocarbons selectivity over H-Co@NCNHP is exhibited in Fig. S11. When increasing the temperature from 200 to 230 °C, the CO conversion is enhanced from 13.4% to 38.9%, and meanwhile, the C_{5+} selectivities are maintained at ca. 87%. Further raising the temperature to 240 °C, the CO conversion is increased to 49.3%, while the C_{5+} selectivity drops largely to 74.3%. Therefore, the reaction temperature of 230 °C was chosen for further FTS experiments.

The influence of GHSV on FTS performances is also investigated over H-Co@NCNHP (Fig. S12 and Table S2). With an increase in GHSV from 2400 to 32,800 $\text{mL g}_{\text{cat}}^{-1} \text{h}^{-1}$, the CO conversion decreases from 41.1% to 13.4%. Moreover, when the GHSV is higher than 6000 $\text{mL g}_{\text{cat}}^{-1} \text{h}^{-1}$, the

C_{5+} selectivity remains almost unchanged. Impressively, at 28,400 $\text{mL g}_{\text{cat}}^{-1} \text{h}^{-1}$, H-Co@NCNHP achieves a C_{5+} selectivity as high as 90.4%, at a CO conversion of 16.4%. Moreover, as shown in Fig. S13, there is no significant change observed in the C_{5+} hydrocarbons distribution over H-Co@NCNHP under different GHSVs (3600 and 28,400 $\text{mL g}_{\text{cat}}^{-1} \text{h}^{-1}$). The $\text{STY}_{\text{C}_{5+}}$ value of H-Co@NCNHP is $1.67 \times 10^{-5} \text{ mol g}_{\text{cat}}^{-1} \text{s}^{-1}$, particularly, which presents a 27.8-fold improvement as compared with that of S-Co/C prepared by an impregnation-calcination method. The catalytic performances of H-Co@NCNHP are comparable to that of the most active Co-based catalysts reported to date (Table S3 and Fig. 3e). The intrinsic activity of these advanced catalysts was improved via the improved interaction between metallic nanoparticles and reducible oxide supports, the construction of *hcp* Co NPs, [18] the use of noble metals as promoters, [34] or the optimal crystalline facet of cobalt, [35,36] and so on. In this work, the electronic properties of Co-based catalysts are adjusted by the construction of hollow structures, to achieve the enhanced intrinsic activity.

3.3. Analysis of the high catalytic activity of H-Co@NCNHP

To gain insights into the excellent catalytic performances of H-Co@NCNHP, S-Co@NCNHP, H-Co@NCNHP, S-Co@NCSP, and S-Co/C

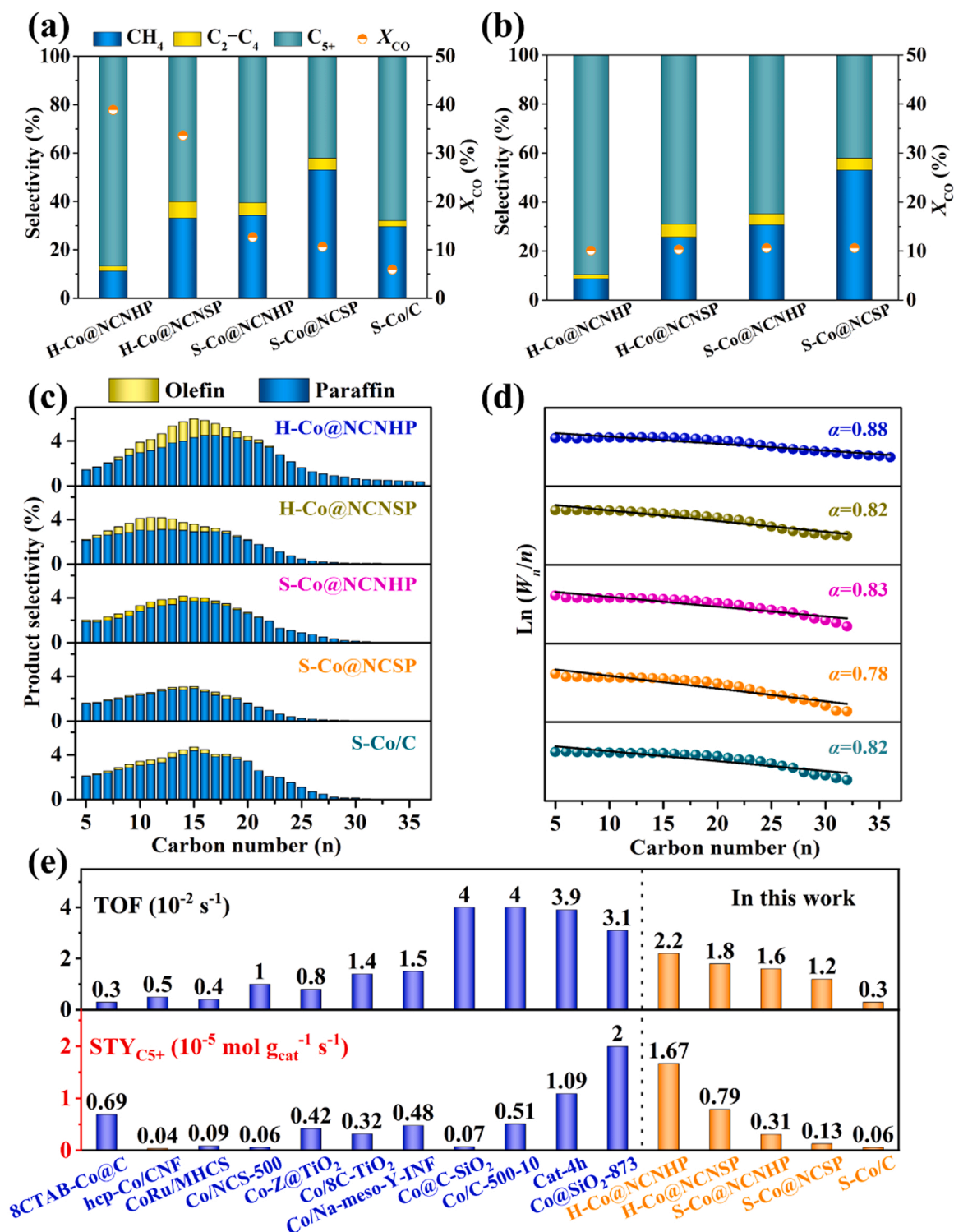


Fig. 3. (a) FTS catalytic performances, (b) hydrocarbons selectivities under the similar CO conversion (ca. 10.5%), (c) detailed hydrocarbons (C₅+) distribution, and (d) the carbon chain growth probability (α) over different catalysts. (e) Comparison of TOF and STY_{C5+} of the catalysts reported in the literature and in this work. Reaction conditions: (a, c, d) 230 °C, H₂/CO = 2, 2.0 MPa, 3600 mL g_{cat}⁻¹ h⁻¹; (b) 230 °C, H₂/CO = 2, 2.0 MPa. Time on stream, 24 h.

were also employed as catalysts in the FTS. The FTS performance data were acquired at 15 h since the FTS reaction started. The internal pore diffusional limitation was quantified by Weisz-Prater criterion (The details are shown in [Supplementary material](#)). The calculated dimensionless values of C_{wp} over H-Co@NCNHP, H-Co@NCNSP, S-Co@NCNHP, S-Co@NCSP, and S-Co/C catalysts are 2.39×10^{-4} , 2.06×10^{-4} , 0.77×10^{-4} , 0.65×10^{-4} , and 0.36×10^{-4} respectively,

all of which are lower than 1 ([Table S4](#)). Therefore, the internal pore diffusion is negligible in these catalysts. As shown in [Fig. 3a](#), the CO conversion over H-Co@NCNHP is about 3 times higher than that over S-Co@NCNHP. The surface Co densities of H-Co@NCNHP and S-Co@NCNHP are 8.3×10^{-4} and 3.1×10^{-4} mol g⁻¹, respectively ([Table 1](#) and [Fig. S14](#)). Hence, a higher surface Co density of H-Co NPs accounts for the significant enhancement of catalytic activity. In

Table 1

Physicochemical properties of different catalysts.

Catalyst	Co content (wt%) ^a	Co size (nm)		H ₂ uptake ($\mu\text{mol g}^{-1}$) ^b	Reducibility (%) ^c	Dispersion (%) ^b	Surface Co density ($10^{-4} \text{ mol g}^{-1}$) ^b
		XRD ^d	TEM ^e				
H-Co@NCNHP	51.4	17.4	17.0	413.9	95	9.1	8.3
H-Co@NCNSP	51.5	10.1	12.4	342.7	96	7.5	6.9
S-Co@NCNHP	33.0	16.1	16.6	154.2	100	5.5	3.1
S-Co@NCSP	24.2	9.6	11.5	127.3	100	6.2	2.5
S-Co/C	15.4	24.0	26.7	165.3	94	11.9	3.3

^a Determined by ICP-OES analysis.^b Calculated from H₂-TPD analysis.^c Calculated from H₂-TPR analysis.^d Determined by XRD using the Scherrer equation.^e Evaluated from TEM images by counting more than 150 Co NPs.

addition, compared with S-Co@NCNHP, H-Co@NCNHP ($2.2 \times 10^{-2} \text{ s}^{-1}$) with similar sizes of Co NPs (ca. 17 nm) achieves a 1.5-fold enhancement in the TOF (Fig. 3e). These results suggest that the H-Co NPs not only reduce the number of buried Co atoms, but also afford superior ability in CO dissociation, which could be further confirmed by the following characterizations and DFT calculations (see Figs. 4 and S15).

As observed in Fig. 4a, the CO-TPD/MS profiles reveal that the desorption temperatures of CO on H-Co NPs are higher than those on S-Co NPs, demonstrating that H-Co@NCNHP and H-Co@NCNSP possess stronger capability in CO adsorption/activation, as compared with S-Co@NCNHP and S-Co@NCSP. To further disclose the interactions between the adsorbed CO and catalysts, projected density of states (pDOS), and projected crystal orbital Hamilton population (pCOHP) were obtained. In Fig. 4b, compared with S-Co, more pDOSs of Co 3d in H-Co are involved in the overlap region with those of C 2p near the Fermi level.

The adsorption energies of CO on the H-Co and S-Co are -1.06 and -0.93 eV (Tables S5-S6), respectively. These results suggest that H-Co has a much stronger interaction with CO. Additionally, the integrated pCOHP (ICOHP) (Fig. 4c) allows quantifying the bond strength of CO itself on the H-Co and S-Co surfaces. A more positive ICOHP is observed for H-Co, indicating that the breakage of C–O is easier than that on S-Co.

In all *d* orbitals (d_{xy} , d_{yz} , d_{xz} , $d_{x^2-y^2}$, and d_{z^2}), the d_{z^2} orbital is perpendicular to the basal plane, which could maximize head-on orbital overlapping with that of reactants, benefiting for the adsorption/activation of them [37]. In Fig. 4d, the detailed pDOS reveals that the contribution of d_{z^2} is predominately determined by the spin-down states for H-Co and S-Co, as evidenced by the d_{z^2} orbital state (spin-down) that crosses the Fermi level (E_f). On the one hand, the up-shifted *d*-band center (ϵ_d) in H-Co with respect to that of S-Co, leads to the decreased occupation of *d* bonding orbitals to make the *d*-5σ (CO) interaction more

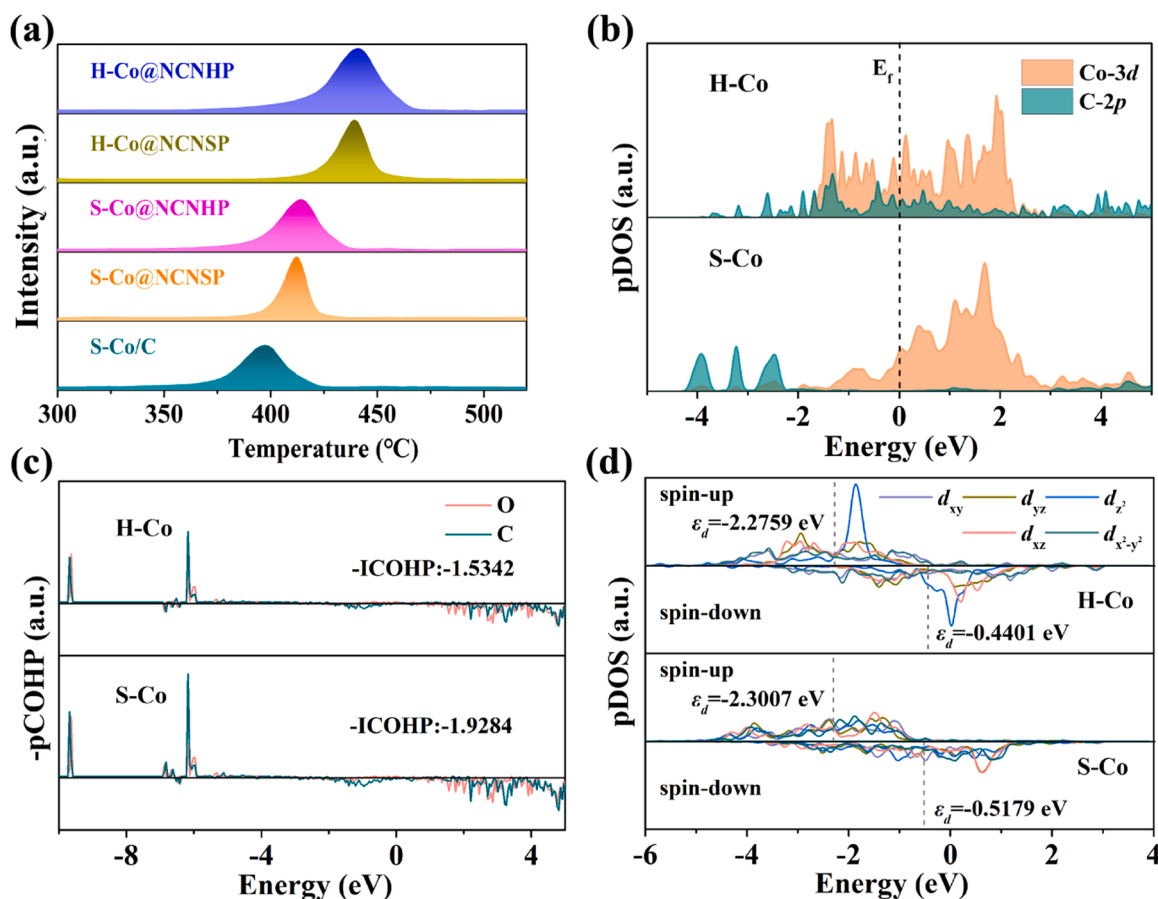


Fig. 4. (a) CO-TPD/MS profiles for various samples. (b) pDOS of CO adsorption on the H-Co and S-Co surfaces. Orange: 3d orbital of Co, cyan: 2p orbital of C. (c) -pCOHP and its integrated value (ICOHP) of CO adsorption on the H-Co and S-Co surfaces. (d) A detailed pDOS for the Co *d* orbitals.

favorable [38]. On the other hand, compared with S-Co, H-Co endows a striking increase in pDOS of d_{z2} antibonding orbital (near E_F), implying an enhanced electron backdonation from the occupied d_{z2} orbitals of metallic Co to the $2\pi^*$ antibonding molecular orbital of CO. All these results provide convincing evidence that the H-Co NPs with synergistic effects of modified empty and occupied d_{z2} orbitals could accelerate the dissociative adsorption of CO [39].

3.4. Analysis of favorable C_{5+} production over H-Co@NCNHP

As shown in Fig. 3a and Table S7, the striking differences in C_{5+} selectivity for the two sets of comparative samples, including H-Co@NCNHP (86.8%) vs H-Co@NCNSP (67.8%) and S-Co@NCNHP (61.2%) vs S-Co@NCSP (42.1%), strongly support the significance of hollow polyhedron structure. The results indicate that the hollow polyhedron serving as a nanoreactor prolongs the contact time between the trapped reaction intermediates and Co active sites, and thus facilitating the growth of long-chain hydrocarbons [33,40]. Specially, the similar CO conversion (ca. 10.5%) is adjusted over H-Co@NCNHP, H-Co@NCNSP, S-Co@NCNHP, and S-Co@NCSP with the GHSVs of 37200, 24000, 4800, and 3600 $\text{mL g}_{\text{cat}}^{-1} \text{h}^{-1}$, respectively. This comparison at the similar CO conversion reveals that there are still evident differences in the C_{5+} selectivities for the four catalysts (Fig. 3b), excluding the possibility affected by the catalytic activity.

The carbon number of long-chain hydrocarbons could go up to 38 over H-Co@NCNHP (Fig. 3c, d), whose carbon growth probability (α) reaches the highest value of 0.88. This result indicates that the hollow polyhedron in H-Co@NCNHP endows a stronger capability in carbon chain growth, which could be further verified by S-Co@NCNHP and S-Co@NCSP with the α values of 0.83 and 0.78, respectively. All these results demonstrate that the hollow polyhedron contributes to the enhanced C_{5+} selectivity. For H_2 and CO activation on Co surface, as reported, H_2 could be easily activated with an energy barrier of ca.

1.5 kJ/mol, whereas that of CO is dozens of times higher. Moreover, the presence of graphitic carbon layers on Co NPs could lead to largely increased coverage degree of H species, and thus obtaining a higher CH_4 selectivity [18].

We also simulated the surface reaction of syngas on different catalysts at 230 °C by using in situ DRIFTS. As observed in Fig. 5, the peaks at 3014 and 2960 cm^{-1} could be ascribed to gaseous CH_4 and $-CH_3$ species, respectively [41]. The peaks at 2926 and 2855 cm^{-1} may be assigned to the stretching vibration of $-CH_2-$ species [42]. When exposed to syngas (solid lines), in all cases, H-Co@NCNHP displays a relatively weak CH_4 peak while strong CH_x peaks, suggesting the lower CH_4 selectivity and higher activity in FTS.

With the purpose of exploring the interactions between CH_x species and Co active sites, the catalysts were then purged in flowing Ar atmosphere for 0.5 h. As shown in Fig. 5 (dashed lines), the CH_4 peaks are still observed over S-Co@NCNHP and S-Co@NCSP, however, there are indiscernible CH_4 signals over H-Co@NCNHP and H-Co@NCNSP. In sharp contrast, the signals of $-CH_3$ and $-CH_2-$ species over S-Co@NCNHP and S-Co@NCSP almost disappear, while the contents of CH_x species decrease only mildly over H-Co@NCNHP and H-Co@NCNSP, particularly over the H-Co@NCNHP. These observations elucidate that the H-Co NPs have stronger interactions with CH_x species, which could stimulate the growth of carbon chain, thus affording higher selectivity towards long-chain hydrocarbons. Collectively, the desirable C_{5+} selectivity over H-Co@NCNHP could be ascribed to the integration of the charming properties of hollow polyhedron and strong interaction between the H-Co NPs and CH_x species.

3.5. FTS mechanism

DFT calculations were performed on the H-Co and S-Co models to gain insights into the reaction mechanism. In general, the transformation of syngas into hydrocarbons mainly involves three steps: the

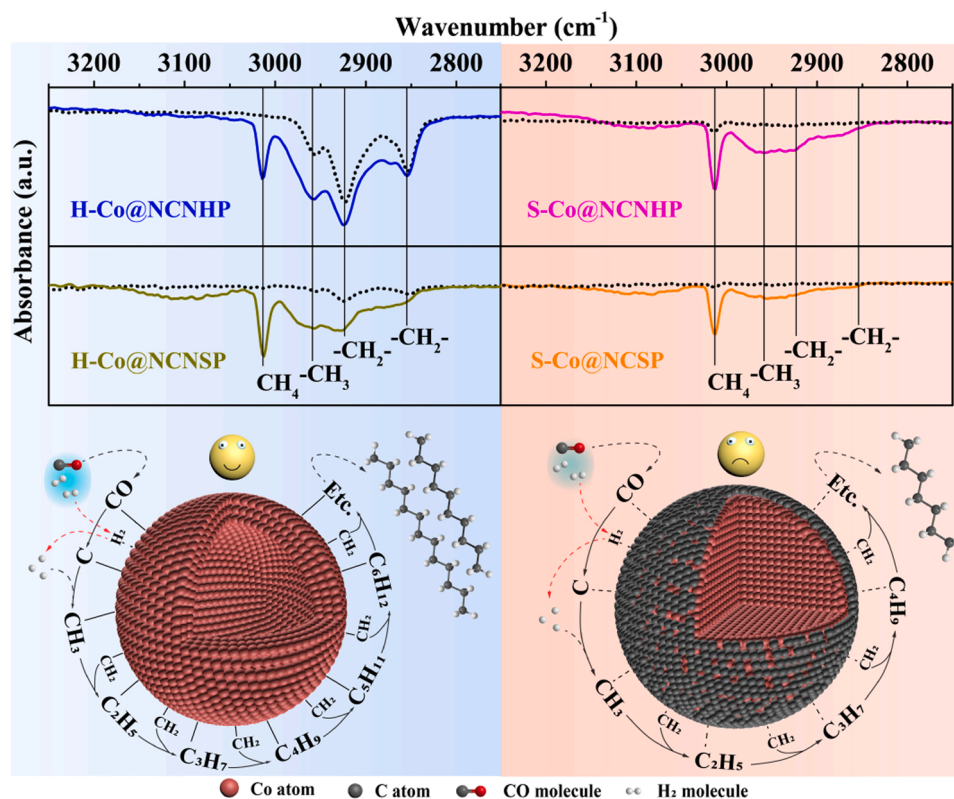


Fig. 5. In situ DRIFT spectra for different catalysts in syngas at 230 °C (solid lines) and purged in Ar for 0.5 h (dashed lines), and schematic illustration of FTS over the H-Co and S-Co NPs.

adsorption and activation of CO/H₂, the hydrogenation of CO to CH_x species, and the growth of carbon chain.

For the activation of CO, the direct CO dissociation and H-assisted CO dissociation were taken into consideration. Within the transformation of H-assisted CO dissociation into CH_x pathways, CHO, CHOH, and CH₂O are suggested as plausible key intermediates on the Co surfaces [43,44]. Herein, top views of the configurations of the initial states (IS), transition states (TS), final states (FS), and energy profiles for them on the H-Co and S-Co surfaces are shown in Figs. 6a and S16–S20. Evidently, all of energy barriers on the H-Co surfaces are lower than those on the S-Co ones (Fig. 6a, b), indicative of a substantial improvement in CO/H₂ activation on H-Co in the FTS process. Furthermore, when H species are present on the H-Co surface, the CO activation is further promoted, as substantiated by the decrease of energy barriers by 0.14–0.25 eV with respect to those on the H-free H-Co surface. All of these results demonstrate that H-Co is beneficial for both direct and H-assisted CO dissociations. Note that the lowest energy barriers of 0.47 and 0.66 eV are gained for C–O bond cleavage of CHOH* over H-Co and S-Co, being the most favorable reaction pathway, respectively, as shown in Figs. 6a and S16–S19. In view of the observations above, we reasonably conceive that CO* + H* → CHO* → CHOH* → CH* + OH* functions as a dominant pathway for the formation of CH species on the Co(111) surface in FTS (Fig. 6c). Also, the adsorption energies of CH* on H-Co and S-Co are −0.72 and −0.68 eV (Tables S5–S6), respectively, which indicates that

the strong capability in bonding CH_x species on the H-Co surface, further verifying the DRIFT spectra observed.

In this FTS process, CHO* + H* → CHOH* is the rate-determining-step with the highest energy barrier of 0.59 eV on H-Co, being lower than that on S-Co (0.73 eV). Simultaneously, to explore the CHO–Co interaction, pDOSs of CHO* adsorption on the H-Co and S-Co surfaces were also calculated. Compared with S-Co, from the pDOS of H-Co in Fig. S21a, more pDOSs of Co 3d are involved in the overlap region with those of C 2p near the Fermi level. Additionally, the ICOHP quantifying the bond strength between CHO* and the H-Co and S-Co (Fig. S21b) implies that a more negative ICOHP is observed for H-Co. These results demonstrate that there is a powerful *d*–*p* coupling between CHO* and H-Co, affording a substantial enhancement in reaction rate.

In the carbon chain growth process, three reaction mechanisms are proposed: carbide mechanism, CO insertion mechanism, and CHO insertion mechanism; and the latter is proposed to be the most favorable on the Co(111) surface, [43] as shown in Fig. 6c. Hence, from C₁ to C₂ products, the C–C coupling (CH* + CHO* → CHCHO*) is the most likely reaction pathway with the energy barriers of 0.36 and 0.49 eV, followed by the breakage of C–O bond (CHCHO* → C₂H₂* + O*) with the energy barriers of 0.21 and 0.23 eV on the H-Co and S-Co surfaces, respectively. Obviously, the energy barriers from C₁ to C₂ on H-Co are lower than those on S-Co, which suggests that the formation of long-chain carbon on H-Co is more facile than that on S-Co, further confirming the reaction and DRIFT results (Figs. 3 and 5).

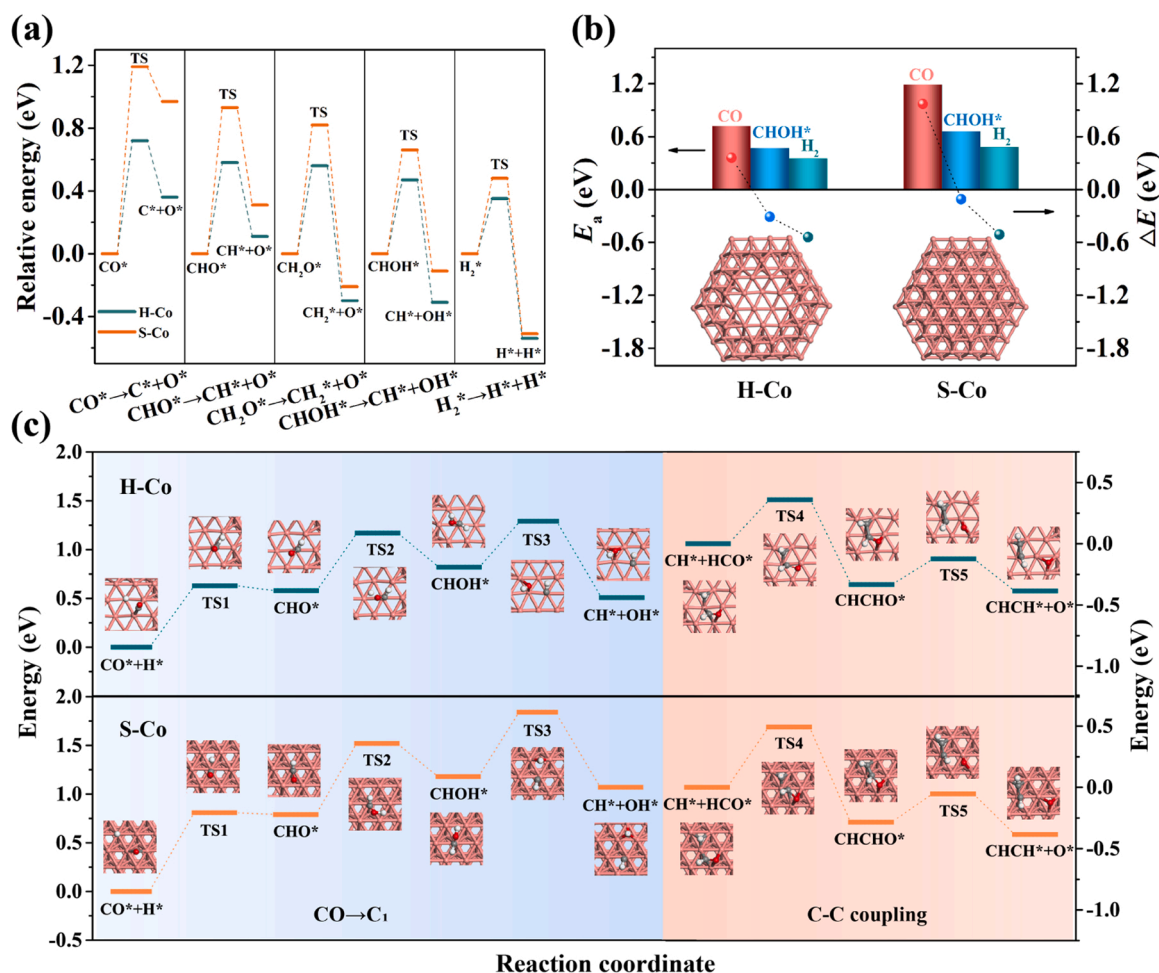


Fig. 6. (a) Energy profiles for direct dissociation of CO, CHO, CH₂O, CHOH and H₂, and (b) energy barriers (histograms) and enthalpies of reaction (dashed lines) for the direct dissociation of CO (red), CHO* (blue), and H₂ (green) on the H-Co and S-Co surfaces. (c) Top views of the configurations at each stage, and potential energy diagram for the conversion of CO to C₁ and C₂ products on the H-Co and S-Co surfaces. The white, grey, red, and pink spheres represent H, C, O, and Co atoms, respectively.

3.6. Stability of catalysts

Other than catalytic activity and selectivity of target products, the stability of catalysts is also of vital significance for the practical applications. H-Co@NCNHP behaves superior stability within 120 h of reaction, wherein the CO conversion and C₅₊ selectivity are remained at around 36% and 86%, respectively, together with a CH₄ selectivity of ca. 12% (Fig. S22). The carbon balance over H-Co@NCNHP is 95.1%. The well-preserved morphology of H-Co@NCNHP is visualized from the TEM images (Fig. S23), showing no obvious aggregation of the H-Co NPs (19.2 nm), which could be ascribed to the semi-encapsulation of H-Co NPs within NCNTs. Intrigued by the excellent catalytic activity and durable stability, the H-Co@NCNHP material holds great promise for potential industrial applications.

4. Conclusion

In summary, we have developed a facile and effective “pyrolysis-oxidation-reduction” strategy to fabricate hollow polyhedrons assembled by N-doped carbon nanotubes with embedded H-Co NPs. Impressively, under 230 °C, 2 MPa, and 28400 mL g_{cat}⁻¹ h⁻¹, H-Co@NCNHP achieves a C₅₊ selectivity as high as 90.4% at a CO conversion of 16.4%. Correspondingly, the STY_{C₅₊} value is 1.67 × 10⁻⁵ mol g_{cat}⁻¹ s⁻¹ over H-Co@NCNHP. Moreover, H-Co@NCNHP shows excellent stability within 120 h of reaction. Systematic characterization data indicate that H-Co NPs show stronger CO/CH_x adsorption than S-Co NPs. DFT results further suggest that the H-Co NPs, which afford modified empty/occupied d_{z2} orbitals and up-shifted d-band center, are beneficial to accelerate the dissociative adsorption of CO and lower the energy barriers of C–C coupling. This work might provide new insights into the rational design of advanced functional materials for various applications in the energy-related fields.

CRedit authorship contribution statement

Yajing Wang, and **Yingwei Li** conceived the research and designed the experiments. **Weiteng Zhan** not only synthesized and characterized most of the catalysts, but also performed the catalytic tests and analyzed the experimental data. **Zhijie Chen**, **Yajing Wang** and **Jianmin Chen** participated in some characterization, reaction experiments, and DFT calculations. **Weiteng Zhan**, **Yajing Wang**, and **Yingwei Li** cowrote the manuscript. All authors participated in the discussion of the results.

Declaration of Competing Interest

The authors declare that they have no known competing financial interests or personal relationships that could have appeared to influence the work reported in this paper.

Acknowledgements

This work was supported by the National Natural Science Foundation of China (21825802, 22138003), the Natural Science Foundation of Guangdong Province (2017A030312005), the Foundation of Advanced Catalytic Engineering Research Center of the Ministry of Education (2020AC006), and the Introduced Innovative R&D Team Leadership of Dongguan City (2020607263005).

Appendix A. Supporting information

Supplementary data associated with this article can be found in the online version at [doi:10.1016/j.apcatb.2022.121469](https://doi.org/10.1016/j.apcatb.2022.121469).

References

- [1] Y. Xu, X. Li, J. Gao, J. Wang, G. Ma, X. Wen, Y. Yang, Y. Li, M. Ding, A hydrophobic FeMn@Si catalyst increases olefins from syngas by suppressing C1 by-products, *Science* 371 (2021) 610–613, <https://doi.org/10.1126/science.abb3649>.
- [2] F. Jiao, J. Li, X. Pan, J. Xiao, H. Li, H. Ma, M. Wei, Y. Pan, Z. Zhou, M. Li, S. Miao, J. Li, Y. Zhu, D. Xiao, T. He, J. Yang, F. Qi, Q. Fu, X. Bao, Selective conversion of syngas to light olefins, *Science* 351 (2016) 1065–1068, <https://doi.org/10.1126/science.aaf1835>.
- [3] A.M. Niziolet, O. Onel, C.A. Floudas, Production of benzene, toluene, and xylenes from natural gas via methanol: process synthesis and global optimization, *AIChE J.* 62 (2016) 1531–1556, <https://doi.org/10.1002/aic.15144>.
- [4] Y. Wang, W. Zhan, Z. Chen, J. Chen, X. Li, Y. Li, Advanced 3D hollow-out ZnZrO@C combined with hierarchical zeolite for highly active and selective CO hydrogenation to aromatics, *ACS Catal.* 10 (2020) 7177–7187, <https://doi.org/10.1021/acscatal.0c01418>.
- [5] J. Li, Y. He, L. Tan, P. Zhang, X. Peng, A. Oruganti, G. Yang, H. Abe, Y. Wang, N. Tsubaki, Integrated tuneable synthesis of liquid fuels via Fischer–Tropsch technology, *Nat. Catal.* 1 (2018) 787–793, <https://doi.org/10.1038/s41929-018-0144-z>.
- [6] Z. Li, Y. Qu, J. Wang, H. Liu, M. Li, S. Miao, C. Li, Highly selective conversion of carbon dioxide to aromatics over tandem catalysts, *Joule* 3 (2019) 570–583, <https://doi.org/10.1016/j.joule.2018.10.027>.
- [7] X. Yang, J. Yang, Y. Wang, T. Zhao, H. Ben, X. Li, A. Holmen, Y. Huang, D. Chen, Promotional effects of sodium and sulfur on light olefins synthesis from syngas over iron-manganese catalyst, *Appl. Catal. B Environ.* 300 (2022), 120716, <https://doi.org/10.1016/j.apcatb.2021.120716>.
- [8] X. Yu, J. Zhang, X. Wang, Q. Ma, X. Gao, H. Xia, X. Lai, S. Fan, T.S. Zhao, Fischer–Tropsch synthesis over methyl modified Fe₂O₃@SiO₂ catalysts with low CO₂ selectivity, *Appl. Catal. B Environ.* 232 (2018) 420–428, <https://doi.org/10.1016/j.apcatb.2018.03.048>.
- [9] C. Hernandez Mejia, T.W. van Deelen, K.P. de Jong, Activity enhancement of cobalt catalysts by tuning metal-support interactions, *Nat. Commun.* 9 (2018) 4459, <https://doi.org/10.1038/s41467-018-06903-w>.
- [10] Q. Cheng, N. Zhao, S. Lyu, Y. Tian, F. Gao, L. Dong, Z. Jiang, J. Zhang, N. Tsubaki, X. Li, Tuning interaction between cobalt catalysts and nitrogen dopants in carbon nanospheres to promote Fischer–Tropsch synthesis, *Appl. Catal. B Environ.* 248 (2019) 73–83, <https://doi.org/10.1016/j.apcatb.2019.02.024>.
- [11] J. Harmel, L. Peres, M. Estrader, A. Berliet, S. Maury, A. Fecant, B. Chaudret, P. Serp, K. Soullantica, hcp-Co nanowires grown on metallic foams as catalysts for Fischer–Tropsch synthesis, *Angew. Chem. Int. Ed.* 57 (2018) 10579–10583, <https://doi.org/10.1002/anie.201804932>.
- [12] Y. Xiang, N. Kruse, Tuning the catalytic CO hydrogenation to straight- and long-chain aldehydes/alcohols and olefins/paraffins, *Nat. Commun.* 7 (2016) 13058, <https://doi.org/10.1038/ncomms13058>.
- [13] M. Javed, S. Cheng, G. Zhang, P. Dai, Y. Cao, C. Lu, R. Yang, C. Xing, S. Shan, Complete encapsulation of zeolite supported Co based core with silicalite-1 shell to achieve high gasoline selectivity in Fischer–Tropsch synthesis, *Fuel* 215 (2018) 226–231, <https://doi.org/10.1016/j.fuel.2017.10.042>.
- [14] C. Xing, P. Ai, P. Zhang, X. Gao, R. Yang, N. Yamane, J. Sun, P. Reubroycharoen, N. Tsubaki, Fischer–Tropsch synthesis on impregnated cobalt-based catalysts: New insights into the effect of impregnation solutions and pH value, *J. Energy Chem.* 25 (2016) 994–1000, <https://doi.org/10.1016/j.jechem.2016.09.008>.
- [15] Y. Zhang, Y. Liu, G. Yang, S. Sun, N. Tsubaki, Effects of impregnation solvent on Co/SiO₂ catalyst for Fischer–Tropsch synthesis: a highly active and stable catalyst with bimodal sized cobalt particles, *Appl. Catal. A Gen.* 321 (2007) 79–85, <https://doi.org/10.1016/j.apcata.2007.01.030>.
- [16] B. Qiu, C. Yang, W. Guo, Y. Xu, Z. Liang, D. Ma, R. Zou, Highly dispersed Co-based Fischer–Tropsch synthesis catalysts from metal–organic frameworks, *J. Mater. Chem. A* 5 (2017) 8081–8086, <https://doi.org/10.1039/c7ta02128c>.
- [17] C. Zhang, X. Guo, Q. Yuan, R. Zhang, Q. Chang, K. Li, B. Xiao, S. Liu, C. Ma, X. Liu, Y. Xu, X. Wen, Y. Yang, Y. Li, Ethyne-reducing metal–organic frameworks to control fabrications of core/shell nanoparticles as catalysts, *ACS Catal.* 8 (2018) 7120–7130, <https://doi.org/10.1021/acscatal.8b01691>.
- [18] Y. Pei, Z. Li, Y. Li, Highly active and selective Co-based Fischer–Tropsch catalysts derived from metal–organic frameworks, *AIChE J.* 63 (2017) 2935–2944, <https://doi.org/10.1002/aic.15677>.
- [19] Q.X. Luo, L.P. Guo, S.Y. Yao, J. Bao, Z.T. Liu, Z.W. Liu, Cobalt nanoparticles confined in carbon matrix for probing the size dependence in Fischer–Tropsch synthesis, *J. Catal.* 369 (2019) 143–156, <https://doi.org/10.1016/j.jcat.2018.11.002>.
- [20] H. Wang, B. Wu, Y. Cai, C. Zhou, N. Feng, G. Liu, C. Chen, H. Wan, L. Wang, G. Guan, Core–shell-structured Co–Zr@TiO₂ catalysts derived from ZIF-67 for efficient production of C₅₊ hydrocarbons in Fischer–Tropsch synthesis, *Ind. Eng. Chem. Res.* 58 (2019) 7900–7908, <https://doi.org/10.1021/acs.iecr.9b00533>.
- [21] Y. Chen, X. Li, M.U. Nisa, J. Lv, Z. Li, ZIF-67 as precursor to prepare high loading and dispersion catalysts for Fischer–Tropsch synthesis: particle size effect, *Fuel* 241 (2019) 802–812, <https://doi.org/10.1016/j.fuel.2018.12.085>.
- [22] X. Sun, A.I.O. Suarez, M. Meijerink, T. van Deelen, S. Ould-Chikh, J. Zecevic, K. P. de Jong, F. Kapteijn, J. Gascon, Manufacture of highly loaded silica-supported cobalt Fischer–Tropsch catalysts from a metal organic framework, *Nat. Commun.* 8 (2017) 1680, <https://doi.org/10.1038/s41467-017-01910-9>.
- [23] Y. Chen, X. Li, J. Zhang, N. Zhao, L. Dai, X. Jiang, C. Liu, S. Lyu, Z. Li, Preparation of SiO₂ immobilized Co-based catalysts from ZIF-67 and the enhancement effect for Fischer–Tropsch synthesis, *Appl. Catal. B Environ.* 289 (2021), 120027, <https://doi.org/10.1016/j.apcatb.2021.120027>.

- [24] Y. Chen, X. Li, L. Dai, M.U. Nisa, C. Liu, S. Lv, J. Lv, Z. Li, Controllable synthesis of core-shell Co@C/SiO₂ catalysts for enhancing product selectivity in Fischer-Tropsch synthesis by tuning the mass transfer resistance, *J. Energy Chem.* 51 (2020) 199–206, <https://doi.org/10.1016/j.jechem.2020.03.074>.
- [25] W. Zhou, K. Cheng, J. Kang, C. Zhou, V. Subramanian, Q. Zhang, Y. Wang, New horizon in C1 chemistry: Breaking the selectivity limitation in transformation of syngas and hydrogenation of CO₂ into hydrocarbon chemicals and fuels, *Chem. Soc. Rev.* 48 (2019) 3193–3228, <https://doi.org/10.1039/c8cs00502h>.
- [26] P. Giannozzi, S. Baroni, N. Bonini, M. Calandra, R. Car, C. Cavazzoni, D. Ceresoli, G.L. Chiarotti, M. Cococcioni, I. Dabo, A. Dal Corso, S. de Gironcoli, S. Fabris, G. Fratesi, R. Gebauer, U. Gerstmann, C. Gougoussis, A. Kokalj, M. Lazzeri, L. Martin-Samos, N. Marzari, F. Mauri, R. Mazzarello, S. Paolini, A. Pasquarello, L. Paulatto, C. Sbraccia, S. Scandolo, G. Sclauzero, A.P. Seitsonen, A. Smogunov, P. Umari, R.M. Wentzcovitch, QUANTUM ESPRESSO: a modular and open-source software project for quantum simulations of materials, *J. Phys. Condens. Matter* 21 (2009), 395502, <https://doi.org/10.1088/0953-8984/21/39/395502>.
- [27] J.P. Perdew, K. Burke, M. Ernzerhof, Generalized gradient approximation made simple, *Phys. Rev. Lett.* 77 (1996) 3865–3868, <https://doi.org/10.1103/PhysRevLett.77.3865>.
- [28] P.E. Blöchl, O. Jepsen, O.K. Andersen, Improved tetrahedron method for Brillouin-zone integrations, *Phys. Rev. B* 49 (1994) 16223–16233, <https://doi.org/10.1103/PhysRevB.49.16223>.
- [29] G. Kresse, D. Joubert, From ultrasoft pseudopotentials to the projector augmented-wave method, *Phys. Rev. B* 59 (1999) 1758–1775, <https://doi.org/10.1103/PhysRevB.59.1758>.
- [30] H.J. Monkhorst, J.D. Pack, Special points for Brillouin-zone integrations, *Phys. Rev. B* 13 (1976) 5188–5192, <https://doi.org/10.1103/PhysRevB.13.5188>.
- [31] Z. Chen, Y. Wang, Q. Liang, L. Chen, W. Zhan, Y. Li, Structure-induced hollow Co₃O₄ nanoparticles with rich oxygen vacancies for efficient CO oxidation, *Sci. China Mater.* 63 (2020) 267–275, <https://doi.org/10.1007/s40843-019-1178-5>.
- [32] M. Xiao, J. Zhu, S. Li, G. Li, W. Liu, Y.P. Deng, Z. Bai, L. Ma, M. Feng, T. Wu, D. Su, J. Lu, A. Yu, Z. Chen, 3d-orbital occupancy regulated Ir-Co atomic pair toward superior bifunctional oxygen electrocatalysis, *ACS Catal.* 11 (2021) 8837–8846, <https://doi.org/10.1021/acscatal.1c02165>.
- [33] Q. Cheng, Y. Tian, S. Lyu, N. Zhao, K. Ma, T. Ding, Z. Jiang, L. Wang, J. Zhang, L. Zheng, F. Gao, L. Dong, N. Tsubaki, X. Li, Confined small-sized cobalt catalysts stimulate carbon-chain growth reversely by modifying ASF law of Fischer-Tropsch synthesis, *Nat. Commun.* 9 (2018) 3250, <https://doi.org/10.1038/s41467-018-05755-8>.
- [34] F. Bertella, C.W. Lopes, A.C. Foucher, G. Agostini, P. Concepción, E.A. Stach, A. Martínez, Insights into the promotion with Ru of Co/TiO₂ Fischer-Tropsch catalysts: an in situ spectroscopic study, *ACS Catal.* 10 (2020) 6042–6057, <https://doi.org/10.1021/acscatal.9b05359>.
- [35] C. Qin, B. Hou, J. Wang, Q. Wang, G. Wang, M. Yu, C. Chen, L. Jia, D. Li, Crystal-plane-dependent Fischer-Tropsch performance of cobalt catalysts, *ACS Catal.* 8 (2018) 9447–9455, <https://doi.org/10.1021/acscatal.8b01333>.
- [36] C. Qin, B. Hou, J. Wang, G. Wang, Z. Ma, L. Jia, D. Li, Stabilizing optimal crystalline facet of cobalt catalysts for Fischer-Tropsch synthesis, *ACS Appl. Mater. Interfaces* 11 (2019) 33886–33893, <https://doi.org/10.1021/acsaami.9b10174>.
- [37] R. Gao, J. Wang, Z.F. Huang, R. Zhang, W. Wang, L. Pan, J. Zhang, W. Zhu, X. Zhang, C. Shi, J. Lim, J.J. Zou, Pt/Fe₂O₃ with Pt-Fe pair sites as a catalyst for oxygen reduction with ultralow Pt loading, *Nat. Energy* 6 (2021) 614–623, <https://doi.org/10.1038/s41560-021-00826-5>.
- [38] Z. Zeng, L.Y. Gan, H. Bin Yang, X. Su, J. Gao, W. Liu, H. Matsumoto, J. Gong, J. Zhang, W. Cai, Z. Zhang, Y. Yan, B. Liu, P. Chen, Orbital coupling of hetero-diatom nickel-iron site for bifunctional electrocatalysis of CO₂ reduction and oxygen evolution, *Nat. Commun.* 12 (2021) 4088, <https://doi.org/10.1038/s41467-021-24052-5>.
- [39] G. Meng, J. Sun, L. Tao, K. Ji, P. Wang, Y. Wang, X. Sun, T. Cui, S. Du, J. Chen, D. Wang, Y. Li, Ru₁Co₉ single-atom alloy for enhancing Fischer-Tropsch synthesis, *ACS Catal.* 11 (2021) 1886–1896, <https://doi.org/10.1021/acscatal.0c04162>.
- [40] V. Subramanian, K. Cheng, C. Lancelot, S. Heyte, S. Paul, S. Moldovan, O. Ersen, M. Marinova, V.V. Ordonsky, A.Y. Khodakov, Nanoreactors: an efficient tool to control the chain-length distribution in Fischer-Tropsch synthesis, *ACS Catal.* 6 (2016) 1785–1792, <https://doi.org/10.1021/acscatal.5b01596>.
- [41] S. Lyu, Q. Cheng, Y. Liu, Y. Tian, T. Ding, Z. Jiang, J. Zhang, F. Gao, L. Dong, J. Bao, Q. Ma, Q.H. Yang, X. Li, Dopamine sacrificial coating strategy driving formation of highly active surface-exposed Ru sites on Ru/TiO₂ catalysts in Fischer-Tropsch synthesis, *Appl. Catal. B Environ.* 278 (2020), 119261, <https://doi.org/10.1016/j.apcatb.2020.119261>.
- [42] Y. Zhang, X. Su, L. Li, H. Qi, C. Yang, W. Liu, X. Pan, X. Liu, X. Yang, Y. Huang, T. Zhang, Ru/TiO₂ catalysts with size-dependent metal/support interaction for tunable reactivity in Fischer-Tropsch synthesis, *ACS Catal.* 10 (2020) 12967–12975, <https://doi.org/10.1021/acscatal.0c02780>.
- [43] M. Yu, L. Liu, Q. Wang, L. Jia, J. Wang, D. Li, B. Hou, Rediscovering tuning product selectivity by an energy descriptor: CH₄ formation and C₁–C₁ coupling on the FCC Co surface, *J. Phys. Chem. C* 124 (2020) 11040–11049, <https://doi.org/10.1021/acs.jpcc.0c02537>.
- [44] C. Chen, Q. Wang, G. Wang, B. Hou, L. Jia, D. Li, Mechanistic insight into the C₂ hydrocarbons formation from syngas on fcc-Co(111) surface: a DFT study, *J. Phys. Chem. C* 120 (2016) 9132–9147, <https://doi.org/10.1021/acs.jpcc.5b09634>.